Draft version January 7, 2020
Typeset using LaTeX **manuscript** style in AASTeX62

Chaos and Resonance in the Inner Stellar Halo from the Galactic Bar

Samuel Moore[1]

[1]*Department of Astrophysical Sciences, Princeton University*

ABSTRACT

This paper investigates the resonant and chaotic orbit structure of orbits in a barred galaxy such as our Milky Way consisting of a flat disc modelled by a Miyamoto-Nagai Potential, a bar modelled by a Long-Murali Potential, and a dark matter halo modelled by a Navarro-Frank-White (NFW) potential. Specifically, this paper computes a chaos indicator by integrating orbits over a set time period and computing orbital frequencies in the first and second half of this period, which can then be used to determine how stable or chaotic an orbit is. From this, the distribution of chaotic orbits in real space is plotted for varying Jacobi Energies in both the x-y and x-z plane, which in turn can be used to search for various resonant orbits and to assess their stability, including Lindblad resonances. The models used in this paper have applications to the analysis of chaotic dispersal of tidal debris, the analysis of moving groups, as well as the constraint of the dark matter distribution of the Milky Way, which are prospective future areas of research.

Keywords: Lindblad Resonances, NFW Potential, Orbital Frequency, Chaos Indicator, Jacobi Energy, Moving Groups

1. INTRODUCTION

There are many different types of galaxies that have been observed in our universe, and have been categorised into Hubble's Tuning Fork. One type of galaxy that is of particular interest to

astrophysicists is the barred spiral galaxy, given that our own Milky Way galaxy is an Sbc type galaxy. (Bland-Hawthorn & Gerhard, 2017)

As a brief summary, spiral galaxies have a number of features. Spiral galaxies consist of a flat rotating disc with includes multiple arms where star formation is highest, a stellar bulge in the centre of the galaxy, and a large dark matter halo which although has not been directly observed, has been predicted by a large amount of evidence including galaxy velocity curves, as well as other evidence which suggests that the ΛCDM model is the best cosmological model for our universe. Spiral galaxies also contain multiple globular clusters that surround the disc, although these are less important when modelling the gravitational potential of a spiral galaxy. (Ryden, 2003)

There is significant evidence to suggest that the bulge of our galaxy is in fact a bar, including evidence from the NIR light distribution, source count asymmetries, gas kinematics, and large microlensing optical depth (A good review of all of this evidence is provided in Gerhard, 2002. Other useful papers include Kuijken, 1996; and Binney, 1994). However, the nature of the bar is still a subject of discussion among astrophysicists.

Spiral galaxies make up approximately 60% of galaxies in our universe, while about two-thirds of these are predicted to contain a bar. Strong bars are clearly visible in 25% to 30% of disk galaxies (Masters et al. 2010). The bar of our Milky War itself has been found to have numerous properties. For example, analysis suggests that the bar must be fairly strong with an inner Lindblad Resonance shown by a peak in longitude=velocity diagrams and as a consequence of this elongated orbits are forced away from the centre, causing the highest streaming velocities induced by the bar to occur a significant distance away from the centre. (Weiner & Sellwood, 1999) In addition, N-body simulations have established that there exist a large number of resonant orbits. (Combes & Sanders, 1981)

Understanding the resonant and chaotic orbit structure is imperative to further understand the Milky Way. Some fraction of the inner galaxy is made up of disrupted globular clusters, and the timescale over which the debris from these systems mix will depend on how chaotic the orbit structure is. The overall amount of chaos in the disc (i.e. around the solar radius) will change how fast open clusters and stellar associations mix. In addition, resonances can cause over-densities in phase-space

that have been interpreted as moving groups. A number of moving groups have been identified and discussed in Eggen, 1996. From Dehnen, 1997, the distribution of moving groups obeys an asymmetric drift relation and older groups appear on non-circular orbits, which is surprising. Dehnen provides a possible explanation for moving groups on eccentric orbits: A cluster of stars is born onto a near-circular orbit similar to those of the molecular gas. The stars might then be trapped into a resonance with a nonaxisymmetric force field like that of the Galactic bar. If this field slowly evolves, the resonances are shifted in orbit space and the stars trapped. Dehnen, 1997 concludes that to interpret properly the results of his paper, we clearly need a better understanding of the processes potentially involved in the dynamical evolution of the solar neighbourhood, in particular with regard to the effect of orbital resonances, as well as forcing by regular non-axisymmetric components of the gravitational potential, like the central bar. The paper also predicts that resonant orbits will lead to a different behaviour than non-resonant orbits. As a result, investigating resonance due to the Milky Way bar will be useful for future research into moving groups, and may help expand upon the above research.

2. POTENTIAL

We start by reviewing potential theory and its utility for dynamical studies. Given a particle of mass m in a gravitational field, the force exerted upon that particle is given by.

$$\vec{F}(x) = m\vec{g}(x) \tag{1}$$

From Newton's law of gravitation:

$$\delta\vec{F}(x) = Gm\frac{\vec{x}' - \vec{x}}{|\,\vec{x}' - \vec{x}|^3}\rho(x)d^3\,\vec{x}' \tag{2}$$

From this, $\vec{g}(x)$ is defined as:

$$\vec{g}(x) = \int G\frac{\vec{x}' - \vec{x}}{|\,\vec{x}' - \vec{x}|^3}\rho(x)d^3\,\vec{x}' \tag{3}$$

The gravitational potential Φ, can then be defined as

$$\Phi(x) = \int G\frac{\rho(x)}{|\,\vec{x}' - \vec{x}|}d^3\,\vec{x}' \tag{4}$$

By taking the divergence of $\vec{g}(x)$ and noting that $\vec{g}(x) = -\nabla\Phi$, the following equation can be derived:

$$\nabla^2\Phi = 4\pi G\rho \tag{5}$$

This is Poisson's Equation, which provides a useful method of finding the potential Φ if the density profile ρ is known, given a boundary condition. For a more detailed derivation of these formulae, see Binney and Tremaine, 2008. Poisson's Equation is useful because as total galactic mass distribution can be decomposed into a sum of density distributions, then the potential can be expressed as the sum of the potential components.

The potential can then be related to the mass profile by the equation:

$$\Phi = -G\int_r^\infty dr\frac{M(r)}{r^2} \tag{6}$$

In order to construct the total potential of the Milky Way galaxy, it is necessary to consider the major structural components of the galaxy: The bar, the disc, and the dark matter halo. The bar is modelled using the non-axisymmetric Long-Murali Potential (Long & Murali, 1991), which is a triaxial bar with the complicated potential term:

$$\Phi(x,R) = -\frac{GM}{2a}\int_{-a}^{a}\frac{dx'}{[(x-x')^2+y^2+(b+\sqrt{c^2+z^2})^2]^{1/2}} \tag{7}$$

The disc is modelled using the axisymmetric Miyamoto-Nagai Potential (Miyamoto & Nagai, 1975) which applies to flattened mass distributions. The Miyamoto-Nagai potential is given by:

$$\Phi = -\frac{GM}{\sqrt{R^2+(a+\sqrt{z^2+b^2})^2}} \tag{8}$$

The dark matter halo is modelled as an axisymmetric Navarro-Frenk-White (NFW) profile

The NFW model is an example of a two-power density model

$$\rho(r) = \frac{\rho_o}{\frac{r}{R_s}^\alpha(1+\frac{r}{R_s})^{\beta-\alpha}} \tag{9}$$

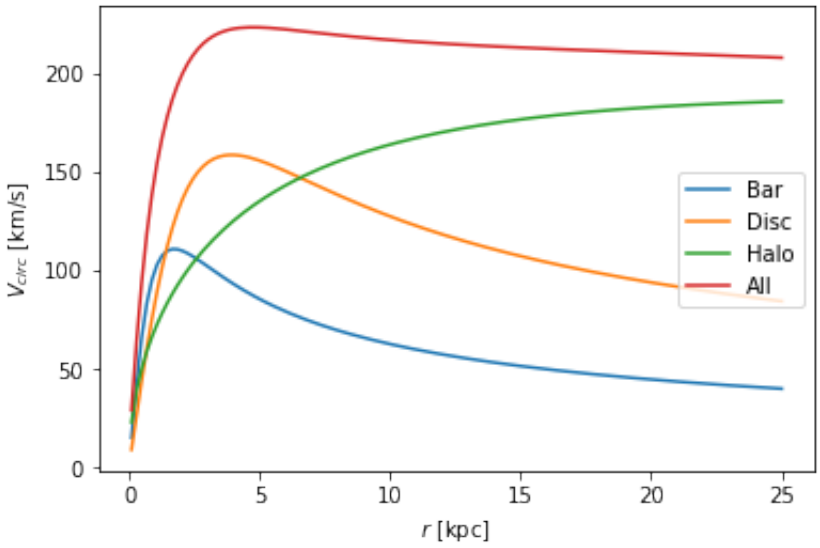

Figure 1. This figure shows the velocity curves for each galactical component. This is calculated using the virial theorem, $V(r) = \sqrt{\frac{2GM(r)}{r}}$

where $\alpha \approx 1$ to 1.5 (in this case, we have let $\alpha = 1$), and $\beta \approx 3$ (Navarro, Frenk and White, 1996), and thus the density is given by the following equation:

$$\rho(r) = \frac{\rho_o}{\frac{r}{R_s}(1 + \frac{r}{R_s})^2} \tag{10}$$

resulting in the following NFW potential:

$$\Phi = \frac{-4\pi G \rho_o R_s^2 ln(1 + r/R_s)}{r/R_s} \tag{11}$$

The individual gravitational potentials of each component can then be superimposed to form a complete model of a barred galaxy with a dark matter halo. Figure 1 shows the circular velocity curves of each of these galactic components, which is a function of their mass profiles.

3. FUNDAMENTAL FREQUENCIES

Angle-action coordinates are a set of canonical coordinates that are of particular use in orbital mechanics. In the general case, the canonical transformation from local coordinates (q,p) to action-angle coordinates (Q,P) is given by:

$$P_i = \frac{1}{2\pi} \oint p_i \, dq^i \tag{12}$$

$$Q^i = \frac{\partial}{\partial P_i} \int p_i \, dq^i \tag{13}$$

Following the convention in Binney and Tremaine, we denote action-angle variables as (θ, $\mathbf{J}$), where $\mathbf{J} = (J_1, J_2, J_3)$ and are integrals of motion. As the generalised momenta are constants of motion:

$$\dot{J}_i = \frac{\partial H}{\partial \theta_i} = 0 \tag{14}$$

The Hamiltonian is independent of θ, and Hamilton's Equations can be solved as follows:

$$\dot{\theta}_i = \frac{\partial H}{\partial J_i} \equiv \Omega_i(\mathbf{J}) \tag{15}$$

where $\Omega_i(\mathbf{J})$ are the three fundamental frequencies.

Fundamental frequencies are important as they allow us to define resonance in the form $\mathbf{n} \cdot \mathbf{\Omega} = 0$ where $\mathbf{n} \neq \mathbf{0}$. As a consequence, this suggests that the ratio between two of the frequencies is a rational number, meaning that the generation of frequency ratio plots is a useful way to try and observe resonance.

4. ORBIT GENERATION AND INTEGRATION

With the potential model established, it is now possible to begin generating and numerically integrating orbits. In most systems, it is not possible to compute orbits analytically so numerical integration is required instead. To begin with, it is necessary to establish various parameters for each component of the potential, including mass and semi-major and semi-major axis where relevant (see Table 1). In addition, it is important to note that we are integrating orbits in a rotating frame. As a result, it is also necessary to specify both the rotation frequency, and the rotational axis. The pattern speed, Ω_p, is the angular velocity of the frame of reference in which the potential is static. Ω_p is parametrised by the equation $R = D_L/a_b$ where D_L is the Lagrangian radius at which gravitational and centrifugal forces cancel out in the bar rest frame, and a_b is the semi-major axis of the

bar. D_L can be approximated by the co-rotation radius, R_{CR}. (Debattista, Gerhard & Sevenster, 2002). Numerous methods have been used to estimate the pattern speed of the bar of the Milky Way. For example, Debattista, Gerhard & Sevenster, 2002 determine $\Omega_p = 59 \pm 5$ km s^{-1} kpc^{-1}, Welner and Sellwood, 1999 determine $\Omega_p = 41.9$ km s^{-1} kpc^{-1}, and Fux, 1999 gives a range of $\Omega_p = 30 - 40$ km s^{-1} kpc^{-1}. For our model, we assumed that rotation is $\Omega_p = 40$ km s^{-1} kpc^{-1}, and occurs about the z-axis. Figure 2 shows an orbit in a rotating frame, and its conversion into an inertial frame.

Parameters for Potentials						
Potential	*Type*	m	a	b	c	r_s
Bar	Long-Murali	$1 * 10^{10}$	1.49	0.58	0.4	
Disc	Miyamoto-Nagai	$4.5 * 10^{10}$	2.5	0.28		
Halo	NFW	$6 * 10^{11}$				15

Table 1. A table showing the values of different parameters for each component of the galaxy. A blankspace indicates that the parameter is not required for this particular potential. a, b, and c represent various axis scales (major, intermediate and minor respectively), where for the Long-Murali potential a is the bar half-length. r_s is the scale radius.

In order to integrate the orbit, we use the Dormand-Prince Runge-Kutta 8(5,3) integrator (DOPRI853) (Prince & Dormand 1981). The Dormand-Prince-Runge-Kutta integrator is a non-symplectic and non-reversible integrator that is considered to be a reliable integrator as it operates to eighth-order accuracy. It should be noted that the use of this specific method of numerical integration is rather memory-intensive. In addition, it introduces some degree of error. We desire that the Jacobi Energy should remain constant with each time step as it should, however, plotting $|\frac{E-E_o}{E_o}|$ against the number of time steps produces a line of a non-zero gradient, showing that the Jacobi energy diverges over time (Figure 4). However, given that this divergence is on the scale of 10^{-14} for 1 million time steps, this error is negligible for our purposes.

5. CHAOS INDICATOR AND FREQUENCY

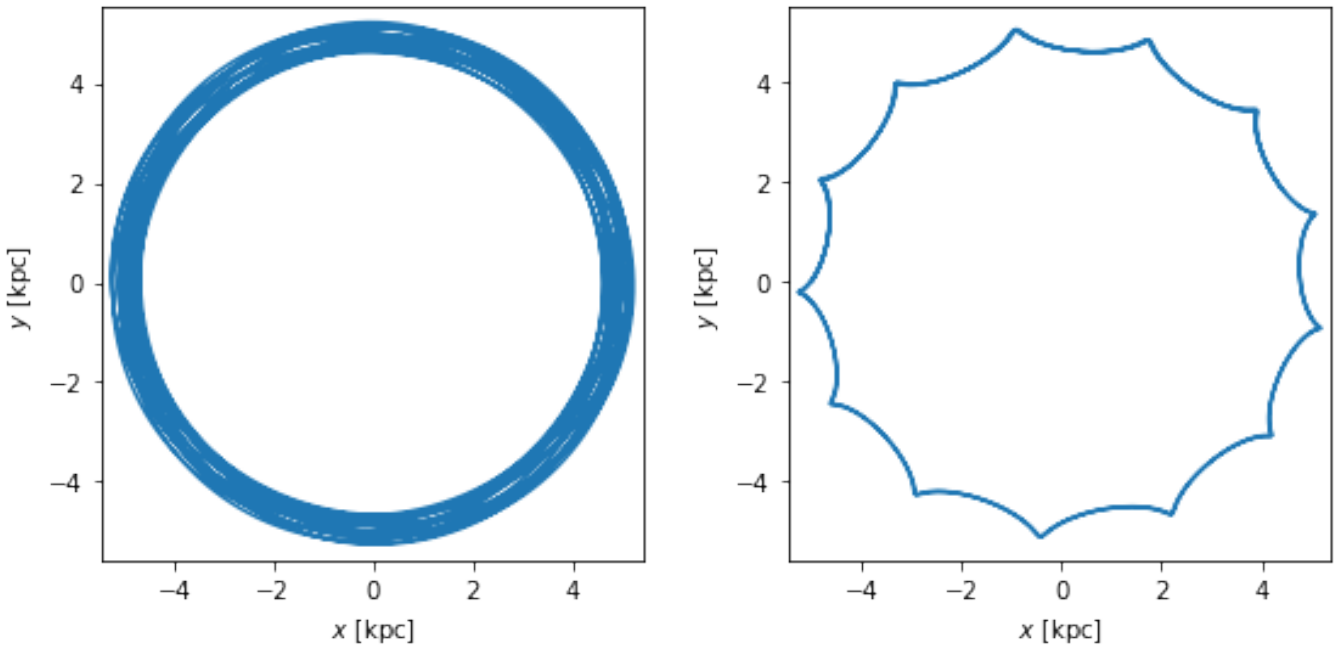

Figure 2. Left: This figure shows the generation of an orbit in x-y space over 20000 time steps where $dt = 0.5$ Myr. Right: This figure shows the conversion of the orbit in Figure 1 into a static reference frame, considering the rotation of the galaxy at $\Omega_p = 40$ km s^{-1} kpc^{-1} about the z-axis.

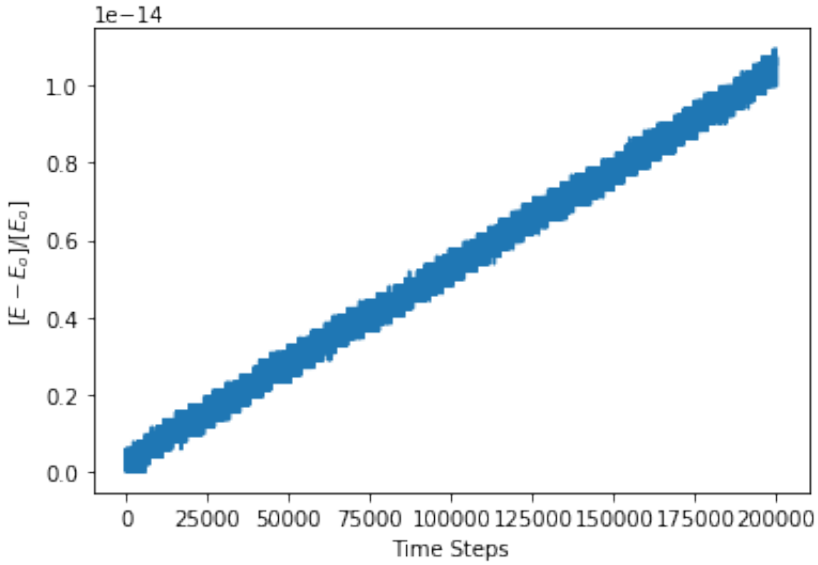

Figure 3. This graph shows the divergence of the orbital energy over each time step when integrating using the DOPRI853 integrator. As this is on the order of 10^{-14}, this is very close to machine precision.

After integrating an orbit over a large number of time steps using the DOPRI853 Integrator, we next calculate a measure of the chaos of this orbit. To do this, the orbit is split into two equal halves. From this, the fundamental orbital frequencies of the first half and the second half can be calculated. These frequencies shall be called $\mathbf{\Omega_1}$ and $\mathbf{\Omega_2}$ respectively. From these frequencies, it is then possible to calculate a measure of the chaos based upon how much these two frequencies differ, given by:

$$\lambda = |\frac{\mathbf{\Omega_2} - \mathbf{\Omega_1}}{\mathbf{\Omega_1}}| \tag{16}$$

The chaos indicator is a strong indicator of the stability of an orbit, and thus is a useful tool for finding resonant orbits. As a rough approximation, chaos values of $\approx 10^{-7}$ are stable, while chaos values of $\approx 10^{-3}$ are chaotic.

6. RESONANCE

Orbital resonance occurs when there is some integer relation between the radial frequency Ω_r, the azimuthal frequency Ω_ϕ, and the bar frequency Ω_p. Resonance occurs more generally when there is an integer relation between the frequency components. In a barred potential, there is an additional type of resonance that involves the pattern frequency. More specifically, Lindblad resonance occurs when

$$m(\Omega_\phi - \Omega_p) = \pm\Omega_r \tag{17}$$

where the positive value corresponds to an inner Lindblad resonance, while the negative value corresponds to the outer Lindblad resonance. In the case where $\Omega_r = 0$, Equation 13 reduces to the co-rotation resonance:

$$\Omega_p = \Omega_\phi \tag{18}$$

Upon identifying a resonant orbit, it is then necessary to classify it as stable or unstable (chaotic).

7. JACOBI GRAPHS

We want to map out the orbit structure of the barred disc galaxy potential in order to observe which orbits are chaotic, resonant, or stable. To do that, we have to decide on grids of orbits to integrate and compute diagnostics for. Because it is too computationally difficult to consider all possible bound orbits, we restrict ourselves to interesting subsets. For a circular restricted three-body problem, the Jacobi integral is the only property that is conserved. As a result, it is a useful variable for investigating orbits. The way we define subsets is to consider grids of orbits that have the same value of the Jacobi energy. We set the value of the Jacobi energy to be similar to a typical disc star, at approximately $E_j = -0.22$, and basic small-scale simulations showed that this was a good value to view the distribution of chaos.

First of all, it is useful to consider a standard value for the Jacobi Energy, before investigating how changing this energy affects the chaos indicator. First of all, we need to calculate V_ϕ for the standard Jacobi Energy. Consider that for an inertial frame, the Lagrangian is given by:

$$\mathcal{L} = \frac{1}{2}|\ddot{x} + \Omega_p \times x|^2 - \Phi(x) \tag{19}$$

From this, the Hamiltonian of the orbit is given by:

$$H_j = p \times \ddot{x} - \mathcal{L} = \frac{1}{2}p^2 + \Phi - \Omega_p \cdot L \tag{20}$$

where H_j is known as the Jacobi integral. From this, the Jacobi energy can be expressed as:

$$E_j = \frac{1}{2}\ddot{x}^2 + \Phi - \frac{1}{2}(\Omega_p \times L) \tag{21}$$

First of all, we desire to model disc-like orbits, where the initial conditions are $z = V_R = V_z = 0$ to view the x-y plane, and we can calculate V_ϕ from the (x,y) grid. These conditions can be used to simplify equation 9. It is possible to vary the value of the Jacobi energy value to values close to the standard value, and determine how this affects the velocity, and thus the distribution of the chaos in real space. Figure 5 shows the effect of varying the Jacobi energy by $\Delta E_j = 10^{-3}$, while Figure 6 shows the effect of varying E_j on a larger scale of $\Delta E_j = 10^{-2}$.

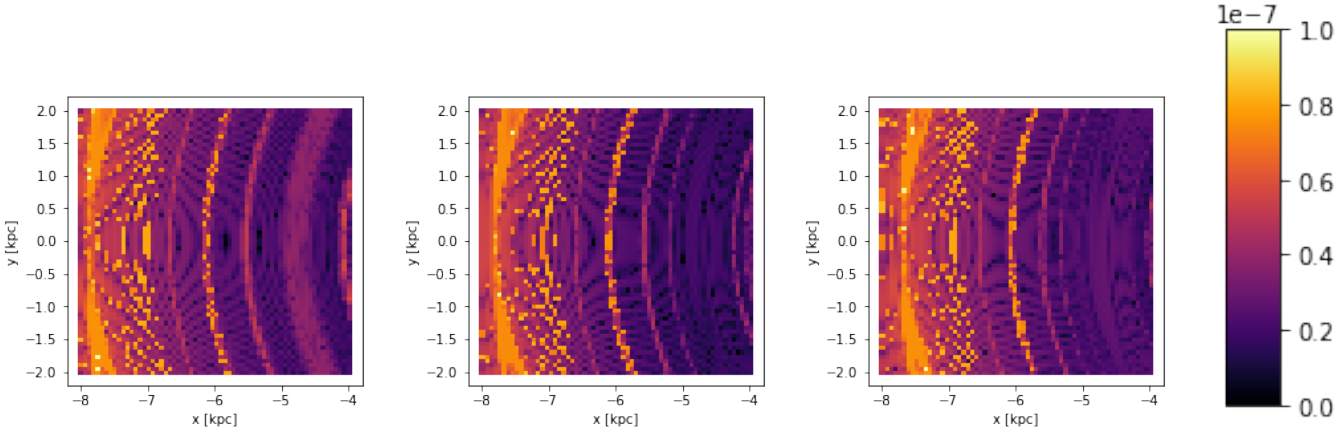

Figure 4. This figure shows the distribution of chaos for disc-like orbits when varying the Jacobi Energy, where $\Delta E_j = 10^{-3}$. Darker, bluer colours represent low chaos, whilst lighter, more yellow colours represent high chaos. Left: $E_j = -0.210 \frac{kpc^2}{Myr^2}$, Centre: $E_j = -0.211 \frac{kpc^2}{Myr^2}$, Right: $E_j = -0.212 \frac{kpc^2}{Myr^2}$

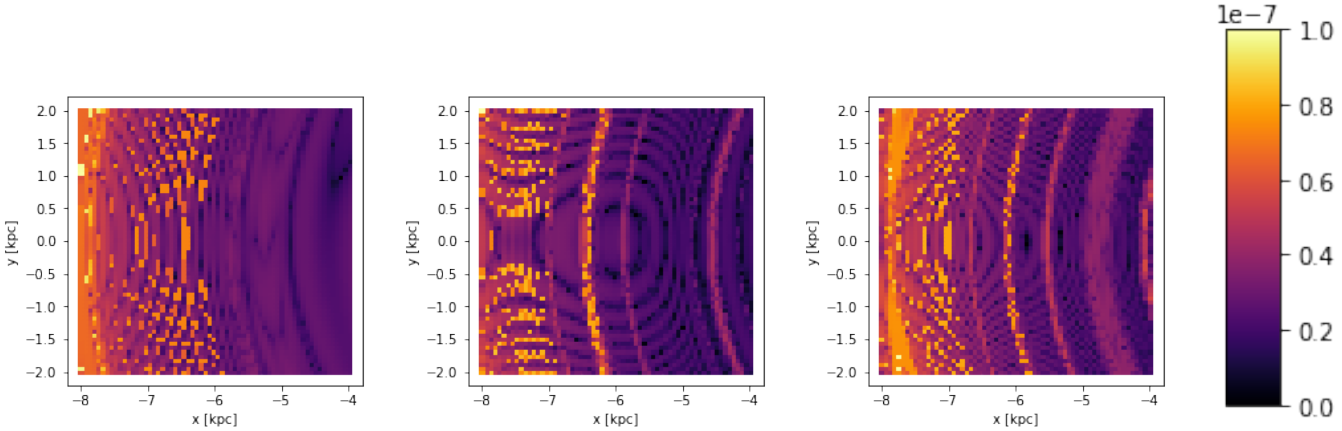

Figure 5. This figure shows the distribution of chaos for disc-like orbits when varying the Jacobi Energy, where $\Delta E_j = 10^{-2}$. Darker, bluer colours represent low chaos, whilst lighter, more yellow colours represent high chaos. Left: $E_j = -0.19 \frac{kpc^2}{Myr^2}$, Centre: $E_j = -0.20 \frac{kpc^2}{Myr^2}$, Right: $E_j = -0.21 \frac{kpc^2}{Myr^2}$

After modelling disc-like orbits, we then modelled halo-like orbits. In a halo-like orbit, we set $y = V_x = V_z = 0$ as the conditions for equation 9, and thus view the x-z plane. Figure 6 shows the effect of varying the Jacobi energy by $\Delta E_j = 10^{-3}$, while Figure 7 shows the effect of varying E_j on a larger scale of $\Delta E_j = 10^{-2}$.

Finally, to help see the bigger picture, two plots were generated over a large scale in both the x-y and x-z plane for $E_j = 0.21$. The graphs are plotted so that the darker, more purple colours

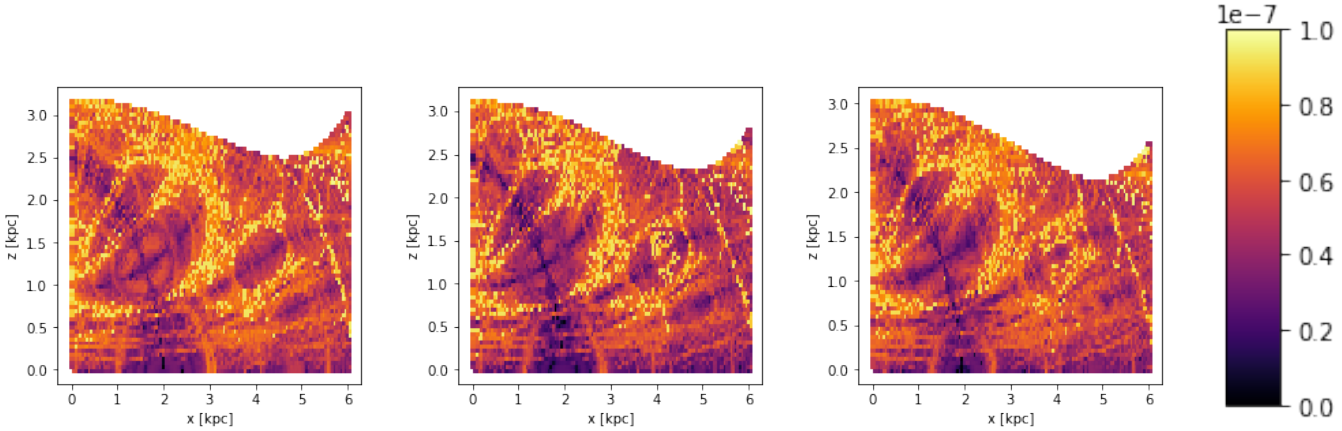

Figure 6. This figure shows the distribution of chaos for halo-like orbits when varying the Jacobi Energy, where $\Delta E_j = 10^{-3}$. Darker, bluer colours represent low chaos, whilst lighter, more yellow colours represent high chaos. Left: $E_j = -0.210 \frac{kpc^2}{Myr^2}$, Centre: $E_j = -0.211 \frac{kpc^2}{Myr^2}$, Right: $E_j = -0.212 \frac{kpc^2}{Myr^2}$

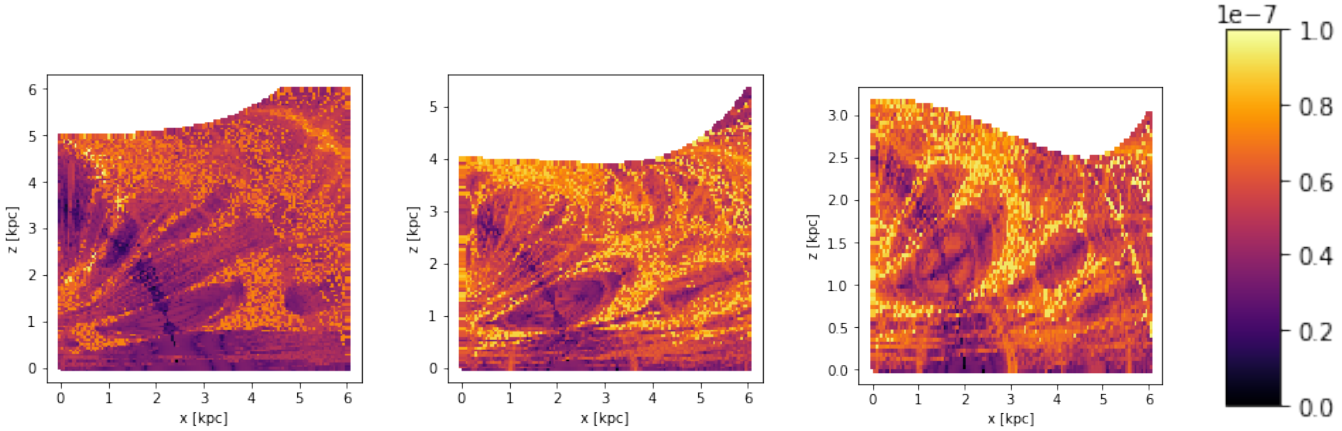

Figure 7. This figure shows the distribution of chaos for halo-like orbits when varying the Jacobi Energy, where $\Delta E_j = 10^{-2}$. Darker, bluer colours represent low chaos, whilst lighter, more yellow colours represent high chaos. Left: $E_j = -0.19 \frac{kpc^2}{Myr^2}$, Centre: $E_j = -0.20 \frac{kpc^2}{Myr^2}$, Right: $E_j = -0.21 \frac{kpc^2}{Myr^2}$

correspond to lower λ values, while more yellow, lighter colours correspond to higher λ values. The observed circular bands of colour correspond to areas where resonant orbits are likely to exist. If the chaos value is lower, then the resonant orbit is likely to be stable, while if the chaos value is higher, then the resonant orbit is likely to be unstable.

Looking in the x-y plane in Figures 4 and 5, it can be seen that making E_j more negative results in a higher level of chaos. This trend seems to also occur in the x-z plane shown in Figures 6 and 7, with

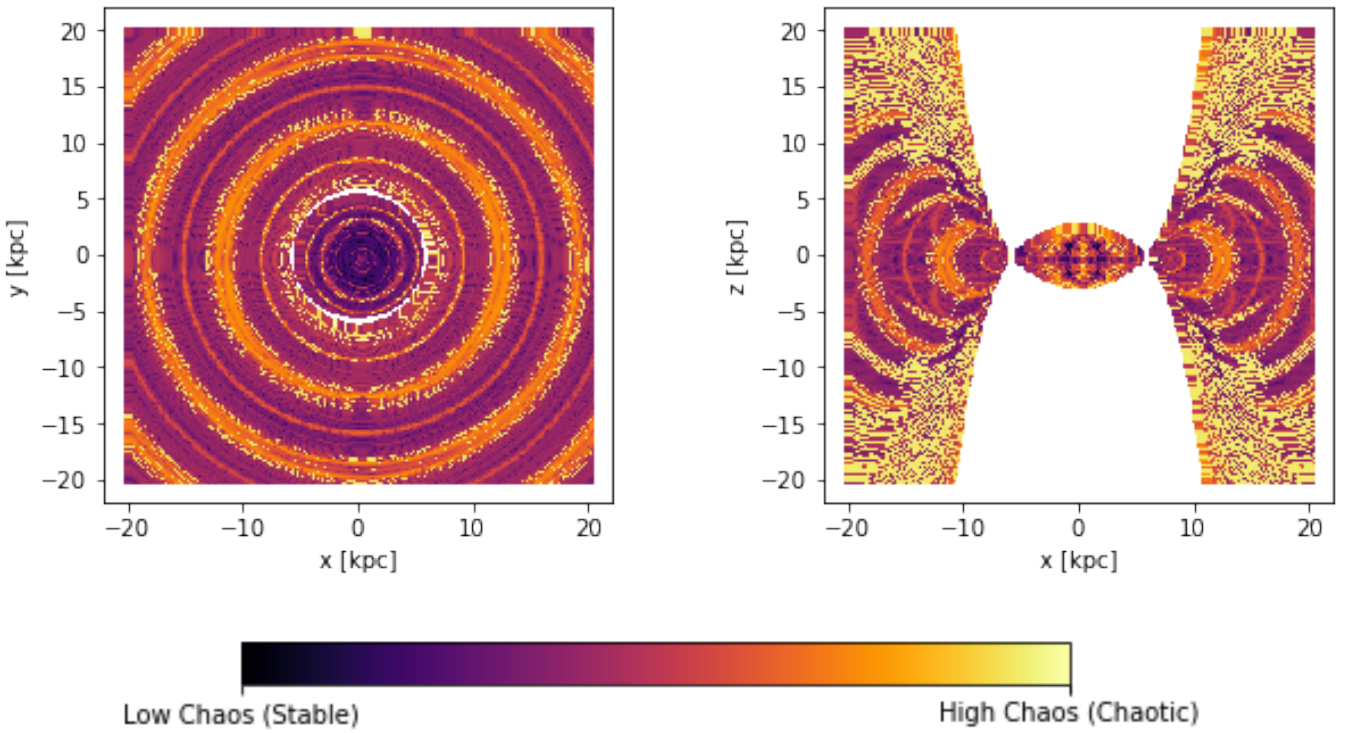

Figure 8. Left: This plot shows a disc-like orbit over a large scale. Right: This plot shows a halo-like orbit over a large scale. Both plots are generated at $E_j = -0.22$ at which point a discontinuity appears, as is expected below a certain value. Darker, bluer colours represent low chaos, whilst lighter, more yellow colours represent high chaos.

various regions becoming more chaotic. In addition, as shown in Figures 6 and 7 by the increase in white space, the orbits become far more bounded even with small decreases in the Jacobi Energy. The fine lines in Figures 4 and 5 are indicative of resonant orbits, and appear to become more dominant as the Jacobi Energy decreases. Figures 6 and 7 show rather clearly the cross-sections of these orbits, especially at the x-axis. These are likely to be indicative of unstable Lindblad resonances.

In addition, it is possible to produce plots of frequencies and frequency ratios plotted against each other to demonstrate resonances. Here, we can plot Ω_2 vs. Ω_1, and $\frac{\Omega_3}{\Omega_1}$ vs. $\frac{\Omega_2}{\Omega_1}$ as shown in Figures 9 and 10 respectively. In Figure 10, straight lines are indicative of frequency ratios that generate resonances, which should be further investigated to check for their stability. Orbits with ratios that deviate from these lines significantly are non-resonant. It should be noted that these plots are

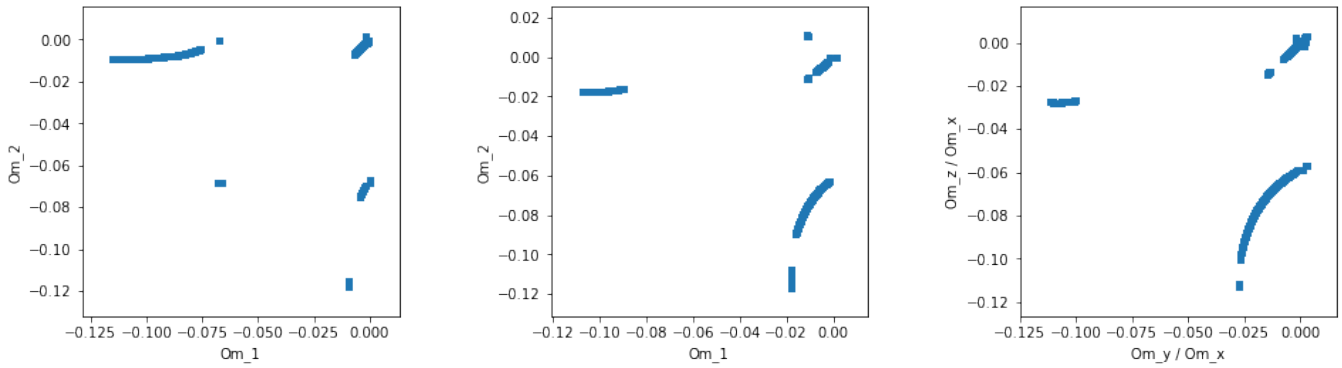

Figure 9. This figure shows the frequency ratios for disc-like orbits when varying the Jacobi Energy, where $\Delta E_j = 10^{-2}$. Left: $E_j = -0.19 \frac{kpc^2}{Myr^2}$, Centre: $E_j = -0.20 \frac{kpc^2}{Myr^2}$, Right: $E_j = -0.21 \frac{kpc^2}{Myr^2}$

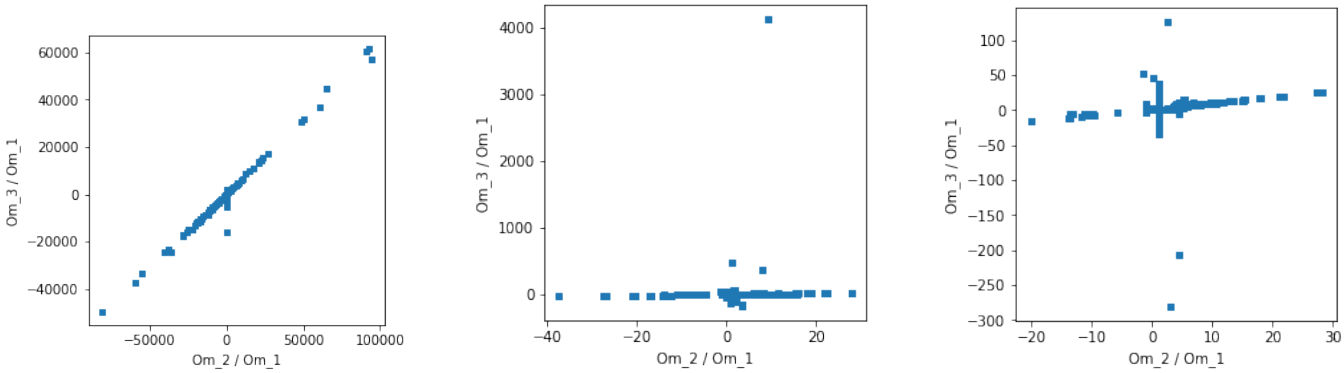

Figure 10. This figure shows the frequency ratios for halo-like orbits when varying the Jacobi Energy, where $\Delta E_j = 10^{-2}$. Left: $E_j = -0.19 \frac{kpc^2}{Myr^2}$, Centre: $E_j = -0.20 \frac{kpc^2}{Myr^2}$, Right: $E_j = -0.21 \frac{kpc^2}{Myr^2}$

preliminary. A point of future investigation is to map out which resonances are dominant using the frequency ratio plots, using a much larger resolution and range to get a higher number of points plotted on the graphs.

8. RESULTS AND CONCLUSION

From the basic results of the Jacobi graphs (Figure 4, 5, 6, 7) and the frequency ratio graphs (Figures 9, 10), it can be concluded that there are a large number of resonant orbits to be investigated across the Jacobi energies that were surveyed. In addition, testing for the stability of each orbit is also necessary as the chaos in real space increases as the Jacobi Energy decreases.

One application of this research into chaos distribution in real space is with regards to tidal streams. Price-Whelan et al. 2015 examines the influence of chaos on the phase-space morphology of cold tidal streams, and suggests that long, cold streams around the Milky Way only exist on regular orbits. These streams in turn may provide a map of the regular regions of the Milky Way potential meaning that tidal stream models could be used to constrain the distribution of dark matter in the Milky Way. Chaotic orbits also have consequences on how fast tidal debris will shear, depending on just how chaotic the orbit is.

There are a number of areas that should be marked for future research. First of all, the model that was used assumes the permanence of the galactic bar. However, it is known that the bar has not always been there, but rather has grown over time. As a result, as the mass profile of the bar has increased over time, the contribution of the bar to the potential has increased. From this, a future improved model should incorporate the varying mass profile by growing the bar over time. Second of all, we sampled orbits from grids. In the future, it would be better to sample orbits from a distribution function in order to make the model more realistic. Finally, given the high variability in the estimation of the pattern speed, Ω_p, it would be valuable to generate plots for a range of pattern speeds as well (e.g: from $\Omega_p = 30 - 65$) to see how varying the pattern speed affects the distribution of chaos.

I would like to thank my advisor Adrian Price-Whelan for all of his help in this project.

I pledge my honor that this paper represents my own work in accordance with University policies. - Sam Moore

APPENDIX

A. NOTES ON COMPUTATION

The process of integrating orbits and generating frequencies can require a large amount of computational work, which can be very time consuming. Table 2 shows the estimated time to generate the Jacobi Graphs for different constraints. In order to reduce the run-time, parallelisation was used to run the code on 4 cores simultaneously, rather than just 1. Running the code on 4 cores instead of 1

approximately reduced the run-time by a factor of 4 which all other constraints equal. Alternatively, this allowed for the grid density to be doubled with no change in the run-time.

Computation Time						
Grid Density	$x1$	$x2$	$y1$	$y2$	Orbit Type	Estimated Time (h:m:s)
128	-2	2	-8	-4	Disc	3:01:34
128	0	6	0	6	Halo	1:37:04
256	-20	20	-20	20	Disc	12:54:21
256	-20	20	-20	20	Halo	8:23:59

Table 2. A table showing the estimated computation time to generate the chaos plots for the above conditions at $E_j = -0.21$ using Intel Core i7-6560U CPU @ 2.20GHz $\times$ 4 without the use of parallelisation. x1 to x2 indicate the start and end points of the x-axis, and y1 and y2 indicate the start and end points of the y-axis or z-axis. The large discrepancy between the completion times for disc plots compared to halo plots is because of the large amount of whitespace generated in the halo plot, for which the code does not generate frequencies.

Run-time remains a current constraint in this paper, and it is recommended that more time is taken to generate plots with higher densities in order to improve the visual quality of the graphs, especially for Figures 4 and 5 (density value = 64). It is recommended that a more powerful computer could be used in order to further reduce run-time when generating plots that require both a large x and y space, and a high grid density.

REFERENCES

Price-Whelan A.M. 2017, The Open Journal, 2, 18

Gerhard. O., 2002, ASP, 273, 73-83

Masters et al., 2010, ASP, 273, 73-83

Welner & Sellwood, 1999, AJ, 524, 112-128

Combes & Sanders, 1981, ASP, 273, 73-83

Long & Murali, 1991, ApJ, 397, 1

Miyamoto & Nagai, 1975, ASJ, 27, 4

Debattista, Gerhard & Sevenster, 2002, ASP, 273, 73-83

Fux R., 1999, A&A, 345, 787

Price-Whelan et al., 2015, RAS, 455, 1079-1098

Prince P. & Dormand J., 1981, Comp. Applied Math, 7, 67

Bland-Hawthorn & Gerhard, 2017, ARAA, 54, 529-596

Navarro, Frenk & White, 1996, ApJ, 462, 563

Kuijken, K., 1995, ASPCS, 91, 504

Eggen, O., 1996, AJ, 112, 4

Dehnen, W., 1998, AJ, 115, 2384-2396

Binney J. (1994) Evidence for a Bar at the Centre of the Milky Way. In: Genzel R., Harris A.I. (eds) The Nuclei of Normal Galaxies. NATO ASI Series (Series C: Mathematical and Physical Sciences), vol 445. Springer, Dordrecht

Binney J. & Tremble S., 2008, Galactic Dynamics: Second Edition. Princeton University Press, Princeton

Ryden, B. Introduction to Cosmology. San Francisco: Addison-Wesley, 2003.